PNAS RESEARCH ARTICLE | APPLIED BIOLOGICAL SCIENCES CHEMISTRY

Fast detection of liver fibrosis with collagen-binding single-nanometer iron oxide nanoparticles via T_1-weighted MRI

Juanye Zhang[a,1], Yingying Ning[b,1], Hua Zhu[a], Nicholas J. Rotile[b], He Wei[c], Himashinie Diyabalanage[d], Eric C. Hansen[a], Iris Y. Zhou[b], Stephen C. Barrett[e], Mozhdeh Sojoodi[e], Kenneth K. Tanabe[e], Valerie Humblet[d], Alan Jasanoff[c], Peter Caravan[b,2], and Moungi G. Bawendi[a,2]

Contributed by Moungi G. Bawendi; received November 29, 2022; accepted March 13, 2023; reviewed by Shouheng Sun and Michael F. Tweedle

SNIO–CBP, a single-nanometer iron oxide (SNIO) nanoparticle functionalized with a type I collagen-binding peptide (CBP), was developed as a T_1-weighted MRI contrast agent with only endogenous elements for fast and noninvasive detection of liver fibrosis. SNIO–CBP exhibits 6.7-fold higher relaxivity compared to a molecular gadolinium-based collagen-binding contrast agent CM-101 on a per CBP basis at 4.7 T. Unlike most iron oxide nanoparticles, SNIO–CBP exhibits fast elimination from the bloodstream with a 5.7 min half-life, high renal clearance, and low, transient liver enhancement in healthy mice. We show that a dose of SNIO–CBP that is 2.5-fold lower than that for CM-101 has comparable imaging efficacy in rapid (within 15 min following intravenous injection) detection of hepatotoxin-induced liver fibrosis using T_1-weighted MRI in a carbon tetrachloride–induced mouse liver injury model. We further demonstrate the applicability of SNIO–CBP in detecting liver fibrosis in choline-deficient *L*-amino acid-defined high-fat diet mouse model of nonalcoholic steatohepatitis. These results provide a platform with potential for the development of high relaxivity, gadolinium-free molecular MRI probes for characterizing chronic liver disease.

liver fibrosis | MRI | contrast agent | iron oxide nanoparticles | targeted delivery

Contrast agents are used in more than 40% of clinical MRI procedures due to their ability to alter MR image contrast in areas where they accumulate by accelerating the relaxation processes of protons in their vicinity (1). Molecular gadolinium-based contrast agents (GBCAs) exhibit strong positive (T_1) contrast enhancement and have achieved significant clinical and commercial success (2). With more than 99% renal clearance, GBCAs are generally considered safe in patients who do not exhibit chronic or acute kidney disease (3, 4). Targeted contrast agents have the potential to profoundly aid disease detection, staging, and prognosis, as well as elucidate complex biology in vivo (5, 6). The development of targeted GBCAs, however, is limited by the sensitivity of the probe and by safety concerns related to gadolinium release and retention (4); micromolar concentrations of GBCAs are usually required for satisfactory MRI resolution, and the safety profiles of targeted GBCAs become debatable at these concentrations, as the residence times of the probes in targeted tissue can be long.

Superparamagnetic iron oxide nanoparticles (SPIONs), including ferumoxytol (an iron replacement therapy approved by the Food and Drug Administration), have emerged as promising competitors to GBCAs (7, 8). SPIONs exceed GBCAs in magnetization per metal ion, making it possible to detect targets at low concentrations in vivo with high sensitivity, albeit by providing negative (T_2) image contrast (9, 10). After imaging, SPIONs were shown to be effectively cleared from the body as they can be metabolized into the endogenous iron pool (11). Although extensive studies have been carried out exploring SPIONs as T_1-weighted MRI contrast agents by controlling the sizes of the nanoparticles and by modifications on the surface (12, 13), most reported SPIONs have high levels of liver accumulation due to phagocytosis by macrophages, or long circulation times in the bloodstream (14). Because of their large (> 6 nm) hydrodynamic sizes, these SPIONs take a long time to extravasate across the endothelium into the interstitial space (hours to days) (15). Phagocytosis leads to high background signal in macrophage-rich organs such as the liver (16), making it challenging to distinguish targeted signals from simple distributions in these tissues; long circulation times and slow extravasation lead to excessively long measurement times of hours or days following administration making the use of targeted SPIONs impractical in the clinic.

Previously, we have engineered both the ligand shell and the inorganic core of SPIONs to improve their properties as T_1 contrast agents. Nonspecific binding between nanoparticles and biomolecules in the plasma was reduced by introducing zwitterionic catechol-based surface ligands (17, 18), and liver uptake of the imaging agents was

Significance

Progress in targeted disease monitoring with MRI has been hindered by the dearth of targeted contrast agents with satisfactory sensitivity, pharmacokinetics, and safety. Combining high per-particle contrast enhancement of nanoparticles and fast pharmacokinetics with high extravasation of small molecules, we constructed SNIO–CBP, a collagen-targeting iron oxide nanoparticle with single-nanometer core size, for diagnosing liver fibrosis. SNIO–CBP exhibits ideal properties as an MRI contrast agent including fast blood elimination, high renal clearance, and minimal nonspecific liver uptake and can achieve comparable sensitivity in liver fibrosis detection to a state-of-the-art gadolinium-based molecular probe within minutes of administration and at a lower dose. Moreover, the SNIO framework is readily adapted to other targeting vectors for broader applications.

Copyright © 2023 the Author(s). Published by PNAS. This article is distributed under Creative Commons Attribution-NonCommercial-NoDerivatives License 4.0 (CC BY-NC-ND).

[1]J.Z. and Y.N. contributed equally to this work.

[2]To whom correspondence may be addressed. Email: pcaravan@mgh.harvard.edu or mgb@mit.edu.

This article contains supporting information online at https://www.pnas.org/lookup/suppl/doi:10.1073/pnas.2220036120/-/DCSupplemental.

Published April 24, 2023.

minimized by limiting the nanocrystal diameter to single-nanometer size (19, 20). With these optimizations, single-nanometer iron oxide nanoparticles (SNIOs) with a zwitterionic coating exhibit a longitudinal relaxivity (r_1) almost identical to that of molecular GBCAs, along with similar tissue-permeability, short circulation times, and comparable clearance profiles (20).

To address an unmet clinical need, here we demonstrate the applicability of targeted SNIOs in the detection of liver fibrosis. Common to most chronic liver diseases (21), liver fibrosis represents scar tissue formation characterized by excess accumulation of extracellular matrix proteins, chiefly collagen (22). Serum biomarkers and elastography methods are useful to detect advanced liver fibrosis, but they are not sensitive enough for the detection of mild to moderate fibrosis (23, 24). Currently, biopsy remains as the only method in the clinic to detect the onset of liver fibrosis. However, biopsies suffer from limitations including sample bias, the risk of complications, and an inability to serially monitor disease progression due to its invasive nature (25). Imaging extracellular collagen through peptide-based collagen-targeting molecular MRI probes was shown to be effective for noninvasive detection and staging of liver fibrosis, but these studies all utilized gadolinium-based probes (26–28, 29).

We demonstrate that functionalization of SNIOs can result in an ideal MRI probe for detecting liver fibrosis. These targeted SNIOs are composed of only endogenous atomic elements, they provide high detection sensitivity at low dosages, and they enable a fast molecular imaging readout following administration. First, we present the stoichiometric functionalization of SNIOs by engineering surface ligands and the development of bioconjugation conditions to incorporate a type I collagen-binding peptide (CBP) to yield SNIO–CBP. We then investigate the biophysical properties of SNIO–CBP, including its affinity toward type I collagen and its pharmacokinetic profile, and compare these characteristics with the state-of-the-art molecular collagen-binding gadolinium-based agent CM-101, which has been demonstrated to be effective in detecting liver fibrosis in various disease models and animal species (28). Finally, we assess the performance of SNIO–CBP in detecting liver fibrosis in two mouse models which resemble toxin- and diet-induced human liver fibrosis.

Results

The synthesis of SNIO–CBP is shown in Fig. 1. Alkyne-functionalized SNIOs (SNIO–alkyne) were prepared through ligand exchange on the SNIO surface (Fig. 1*A*) (20). SNIOs coated with oleic acid (OA), synthesized through thermolysis of iron(III) oleate precursors, were first ligand-exchanged with carboxylic acid ligands modified with oligo(ethylene glycol) to allow for dispersion in mid-polarity solvents such as *N*,*N*′-dimethylformamide (DMF).

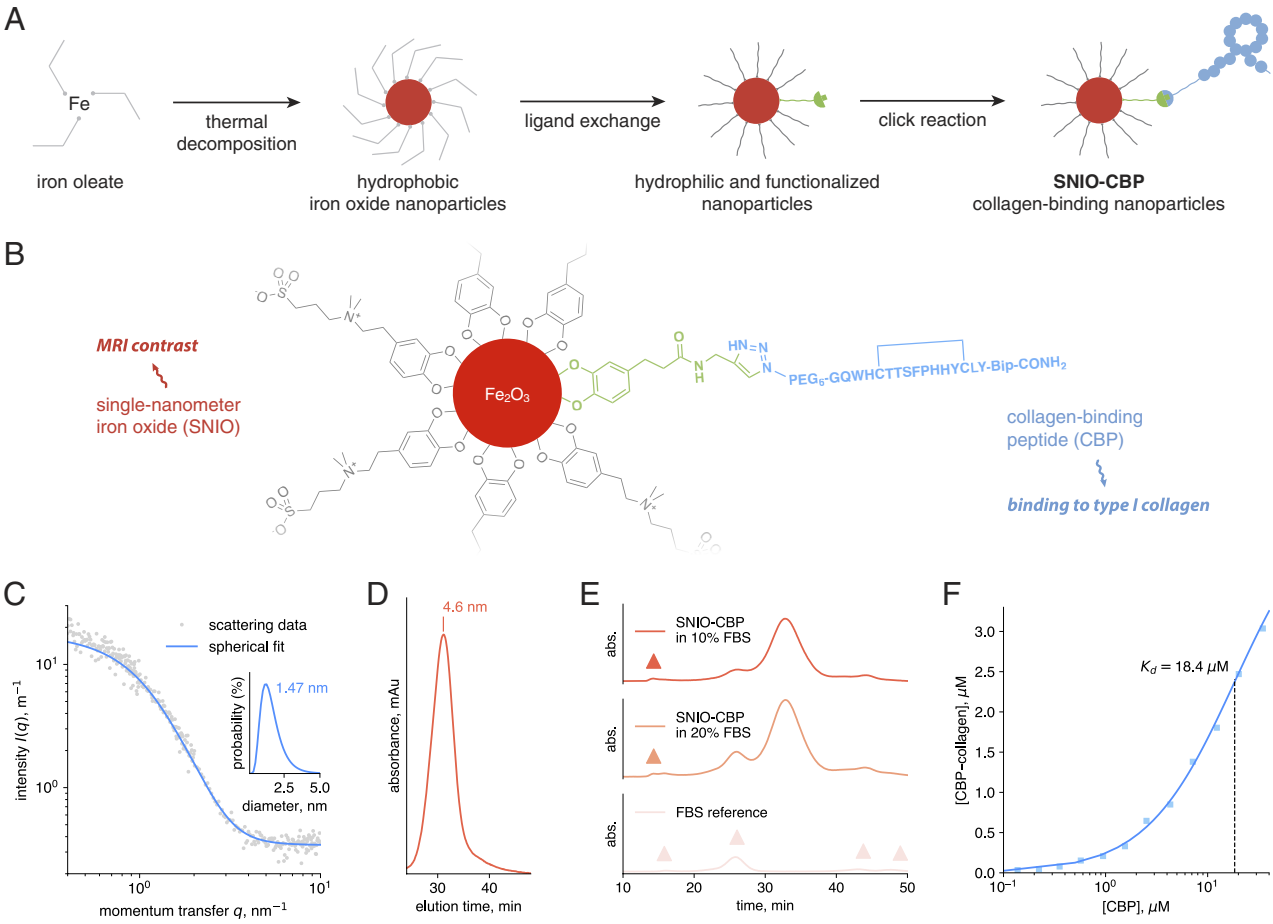

Fig. 1. Synthesis and characterizations of SNIO–CBP. (*A*) Synthesis scheme for SNIO–CBP. (*B*) Schematic illustration of the construction of SNIO–CBP. Two types of ligands are present on the nanoparticle surface: zwitterionic ligands offer stability and solubility, peptide-conjugated ligands allow for targeting. (*C*) SAXS profile of SNIO–CBP in the *q* region corresponding to single-nanometer range in real space; the scattering profile was fitted to spherical particles with a log-normal distribution at a mean diameter of 1.47 nm. (*D*) Gel filtration chromatogram of SNIO–CBP shows its size purity and a hydrodynamic diameter of 4.6 nm. (*E*) Gel filtration chromatograms of SNIO–CBP incubated with two different concentrations of FBS and FBS alone: a minimal degree of nonspecific binding of SNIO–CBP in the plasma were observed. Red and orange peaks: binding products between SNIO–CBP and species in FBS; pink peaks: native species in FBS. (*F*) Binding affinity of SNIO–CBP toward human type I collagen. For the reaction, CBP + collagen ⇌ CBP–collagen, the dissociation constant K_d = 18.4 μM.

Table 1. Longitudinal relaxivities of iron-based SNIO–CBP nanoparticles and gadolinium-based CM-101 molecules

	Longitudinal relaxivity (r_1) at 1.4 T and 37 °C (mM^{-1} s^{-1})		Longitudinal relaxivity (r_1) at 4.7 T and 25 °C (mM^{-1} s^{-1})	
Contrast agent	Per metal ion	Per peptide	Per metal ion	Per peptide
SNIO–CBP	4.5	195	2.7	145
CM-101	11.1	33.3	7.2	21.5

Successive ligand exchanges with a mixture of catechol-based ligands, zwitterionic dopamine sulfonate (ZDS), and propargyl dihydrocaffeic amide (PDA) afforded functionalized water-soluble nanoparticles.

Conjugation between SNIO–alkyne and CBP–azide via a copper-catalyzed alkyne–azide reaction provided the final SNIO–CBP product (Fig. 1*B*): A mixed DMSO–H_2O solvent was used to disperse the hydrophobic CBP–azide, and a nitrogen-based chelating ligand [(benzimidazol-2-yl)methyl]bis[(2-pyridyl)methyl]amine (BPBA) (30) was chosen for its ability to stabilize the Cu(I) catalyst and to accelerate reaction kinetics (31). Considering the catalytic catechol-cleaving ability of iron–BPBA complexes, the conjugation reaction was performed in the absence of oxygen on a Schlenk line (30). After reaction completion, the product SNIO–CBP was precipitated using acetone, redispersed in 10 mM pH 7.4 sodium phosphate buffer, and purified through syringe filtration followed by centrifugal filtration. Solutions of the product proved stable in room air for over a month (*SI Appendix*, Fig. S1).

The size of the iron oxide core in SNIO–CBP was determined by small-angle X-ray scattering (SAXS, Fig. 1*C*) (20, 32). Scattering data were interpreted using a spherical particle model with a log-normal distribution, yielding a mean diameter of 1.5 nm. A mean hydrodynamic diameter of 4.6 nm was obtained by gel filtration chromatography (GFC) (Fig. 1*D*). The CBP ligand shell contributed 3.1 nm to the hydrodynamic diameter, but the size of SNIO–CBP was still below the renal clearance threshold for inorganic nanoparticles (~5.5 nm) (33). Due to the abundance of catechol-based zwitterionic surface ligands, SNIO–CBP showed a near-zero zeta potential of −4.67 mV and exhibited minimal nonspecific binding in plasma after incubation with fetal bovine serum (FBS) (Fig. 1*E*). The hydrophilicity of ZDS provided SNIO–CBP with satisfactory solubility in phosphate buffer up to at least 36 mM on an iron basis or 0.67 mM on a CBP basis (Fe/CBP = 54/1). Assuming a chemical composition of Fe_2O_3 for the iron oxide core, the SNIO/CBP ratio was determined to be 1/1.1 (Supporting Information). Affinity between SNIO–CBP and human type I collagen was investigated in vitro (26, 34), and a collagen-binding dissociation constant K_d = 18.4 μM was measured (Fig. 1*F* and *SI Appendix*).

The r_1 of SNIO–CBP was measured to be 4.5 s^{-1} $(mM\ Fe)^{-1}$ at 1.4 T and 37 °C, 50% higher than unfunctionalized SNIO (3.0 s^{-1} mM^{-1}). The increase in relaxivity was attributed to the reduction of the particle tumbling rate as a result of a 48% larger hydrodynamic diameter. SNIO–CBP and CM-101 (Gd/CBP ratio of 3/1), a gadolinium-based collagen-binding contrast agent (28), shared the same CBP (Table 1). Although CM-101 exhibited a higher r_1 per metal ion, SNIO–CBP showed a 5.9-fold higher r_1 per peptide at 1.4 T due to its higher metal ion/CBP ratio. At 4.7 T, r_1 per peptide for SNIO–CBP was 6.7 times higher than CM-101, providing higher MRI sensitivity without increasing the peptide concentration. The relaxivity of SNIO–CBP was unchanged in the presence of collagen when measured at 4.7 T indicating that further increasing the rotational correlation time upon protein binding provides no further relaxivity benefit. Given previous reports on successfully applying gadolinium-based collagen-binding agents, including CM-101, to various fibrotic animal models (28, 35), these in vitro results suggested SNIO–CBP to be a potential candidate for targeting and imaging fibrosis.

The pharmacokinetics of SNIO–CBP was assessed in healthy male mice using dynamic T_1-weighted MRI (Fig. 2*A*), and the results were quantified by measuring changes in the tissue-to-muscle contrast-to-noise ratio (CNR) in the blood pool (heart), liver, and kidneys. Following intravenous administration (2 nmol SNIO–CBP/gram animal; all animal doses are reported on CBP basis), immediate blood pool enhancement was observed from whole-body MRI with a blood elimination half-life of 5.7 ± 1.9 min that was estimated from a monoexponential decay of the blood pool signal. This half-life was similar to the pharmacokinetics of the gadolinium-based CM-101 (28). The collecting vessels in the kidney were apparent at 1 min post injection (Fig. 2*A*), demonstrating rapid renal filtration owing to the small size of SNIO–CBP (*SI Appendix*, Fig. S2). Importantly, SNIO–CBP only transiently and slightly enhanced the liver (Fig. 2*B*),

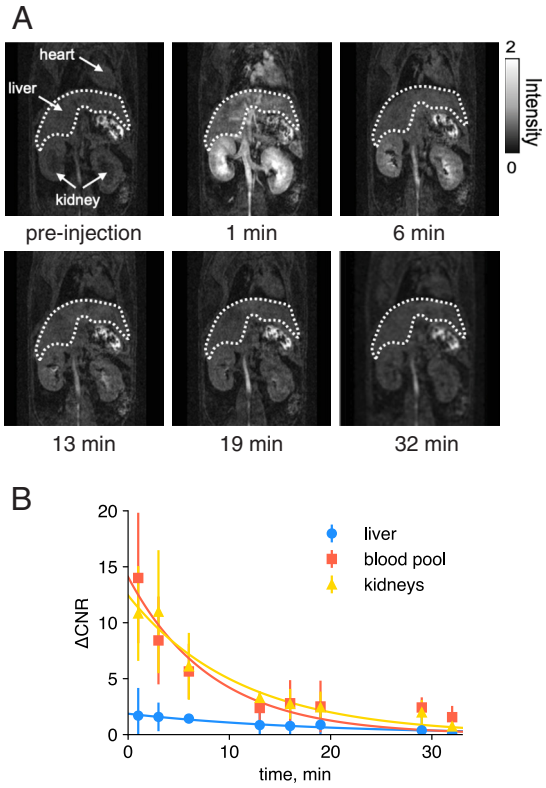

Fig. 2. Clearance profile of SNIO–CBP in normal mice (n = 3). (*A*) Time evolution of T_1-weighted MRI preinjection and up to 32 min postinjection. Signals from the heart, liver, and kidneys were processed for quantification. The dotted curve gives an example of area selection for the liver. (*B*) Clearance profile of SNIO–CBP quantified through CNR in the blood pool, liver, and kidneys. CNR data were fitted into exponential decays. Data shown as mean ± standard deviation (SD).

indicating an extracellular distribution, and implying that the probe was not taken up by liver macrophages.

SNIO–CBP was next evaluated in mice with liver fibrosis induced by 12-wk oral gavage of CCl_4 in olive oil (CCl_4 group), compared to control mice gavaged with olive oil only (OO group) (36). Parallel experiments using CM-101 instead of SNIO–CBP were also carried out (Fig. 3*A*). The probes were administered intravenously with the mouse in the scanner, and T_1-weighted MR imaging was performed preinjection and dynamically up to 35 min postinjection. Doses of 2 nmol/g SNIO–CBP and 5 nmol/g CM-101 were used, and liver-to-muscle CNR was quantified (Fig. 3*B*). Upon injection of SNIO–CBP into CCl_4 injured mice and OO mice, higher liver signal enhancement and persistent liver image contrast were observed in the CCl_4 group compared to the OO group (*SI Appendix*, Fig. S3). A similar trend was observed with CM-101. Due to the faster clearance of CM-101 in the liver, the CNR difference between CCl_4 (2.5 ± 0.5, n = 6) and OO (0.3 ± 0.5, n = 4) groups imaged with CM-101 showed significantly higher liver CNR ($P < 0.0001$) as early as 6 min post injection (Fig. 3*C*). At 13 min postinjection, the average liver CNR of CCl_4 mice (1.8 ± 0.6, n = 6) was also significantly ($P < 0.001$) greater than the average of the control mice (0.4 ± 0.4, n = 4) injected with CM-101. In comparison, a statistical difference between the CCl_4 and OO mice imaged with SNIO–CBP appeared at 13 min ($P < 0.001$). CNR at 13 min postinjection for CCl_4 and OO mice were 1.9 ± 0.2 and 0.9 ± 0.5, respectively. It is worth noting that the average CNR at 13 min postinjection was similar for the two different contrast agents SNIO–CBP and CM-101, despite a 2.5-fold lower dose of the former being administered (Fig. 3*D*). After imaging, animals were sacrificed, and histopathological analyses were performed on the liver tissues.

Collagen staining using Sirius Red showed an increased amount of collagen fibers in CCl_4 mice (Fig. 3*E*). Quantification of the positive staining as collagen proportional area (CPA) was found to be 10-fold higher in the CCl_4 group vs. the vehicle-treated OO group (*SI Appendix*, Fig. S4). Liver hydroxyproline concentration (Hyp), as a quantitative marker of total tissue collagen, also significantly increased after CCl_4 injury (Fig. 3*F*). These data confirmed consistent fibrosis in the CCl_4-injured mice. Accumulation of SNIO–CBP was observed with Prussian Blue staining of iron (Fig. 3*E*). Stained areas showed strong correlation to the locations of collagen in the fibrotic septa (red tracts in the Sirius Red stained slides), further confirming the specific binding affinity of SNIO–CBP to collagen.

SNIO–CBP was then evaluated in a second mouse model of fibrosis. We used a nonalcoholic steatohepatitis (NASH) model caused by choline-deficient, *L*-amino acid–defined, high-fat diet (CDAHFD), which resulted in liver fibrosis with accompanying liver inflammation and steatosis, drawing comparison to NASH in humans (37). Mice were fed CDAHFD (CDAHFD group) or standard chow (SC group) for 14 wk and imaged before and after intravenous 2 nmol/g SNIO–CBP administration (Fig. 4*A*), followed by sacrifice and ex vivo characterization of the liver.

Liver MRI results showed increased liver signal enhancement in CDAHFD mice compared to control SC mice, and this enhancement persisted over time (Fig. 4*B*). At 13 min postinjection, liver-to-muscle CNR in the CDAHFD group (2.1 ± 0.9) was significantly higher than CNR in the control SC group (0.6 ± 0.5) ($P < 0.01$) (Fig. 4*C*). In contrast to the CCl_4 model, Prussian Blue staining of CDAHFD liver tissues showed a highly diffuse distribution of iron (Fig. 4*D*) due to the delocalized and a weblike

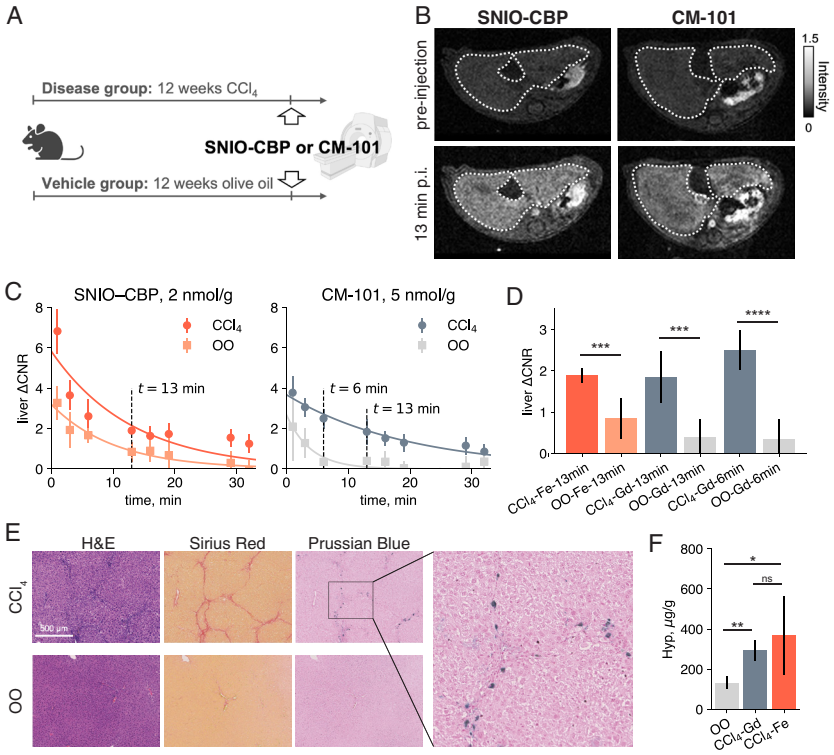

Fig. 3. T_1-weighted MRI of mice with CCl_4-induced liver fibrosis and olive oil vehicle-treated control (OO). (*A*) Schematic illustration of the study design. (*B*) Comparisons of liver MRI signals in CCl_4 mice and OO mice preinjection and 13 min postinjection (p.i.), administered with either SNIO–CBP (2 nmol/g CBP) or CM-101 (5 nmol/g CBP). (*C*) Postinjection MRI signal evolution in liver (n = 6 for each CCl_4 group and n = 4 for OO group). (*D*) Quantified changes in contrast-to-noise ratio CNR of liver at 6 min or 13 min postinjection. Legend: CCl_4–CCl_4 group, OO–OO group, Fe–subjects imaged with SNIO–CBP, Gd–subjects imaged with CM-101, 6min–CNR at 6 min postinjection, 13min–CNR at 13 min postinjection. (*E*) Representative microscopy images of the adjacent liver tissues from CCl_4 (disease) and OO (control) mice, stained with Hematoxylin and Eosin (H&E), Sirius Red, or Prussian Blue. (*F*) Liver collagen concentration assessed by hydroxyproline content (Hyp, μg/g tissue) (n = 6 for each group). All data shown as mean ± SD, *$P < 0.05$, **$P < 0.01$, ***$P < 0.001$, ****$P < 0.0001$, ns: not significant, unpaired t test, two-tailed.

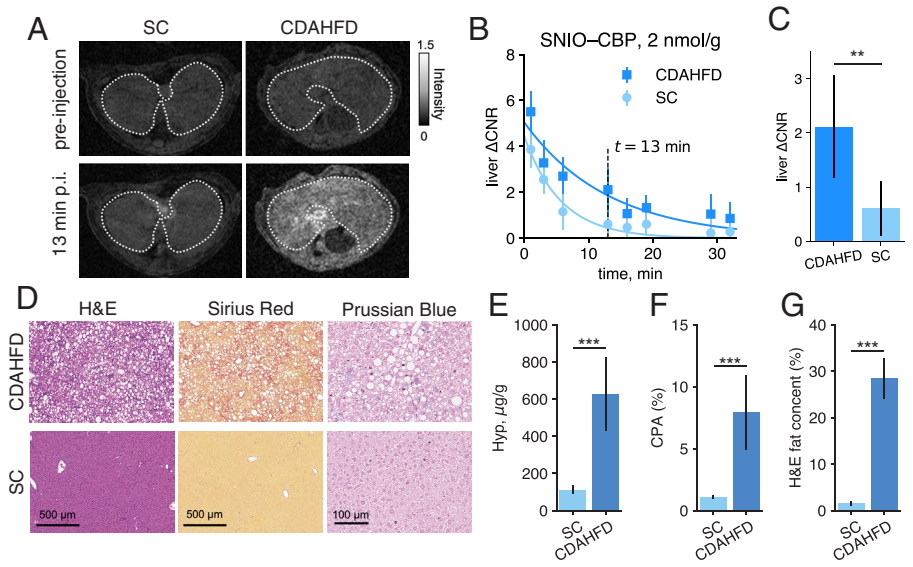

Fig. 4. T_1-weighted MRI of mice fed with choline-deficient *L*-amino acid-defined high-fat diet (CDAHFD) or SC for 14 wk. (*A*) Comparisons of liver MRI signals preinjection and 13 min postinjection (p.i.), administered with SNIO–CBP (2 nmol/g CBP). (*B*) Postinjection MRI signal evolutions in liver. (*C*) Quantified changes in contrast-to-noise ratio of liver at 13 min postinjection. (*D*) Representative microscopy images of the adjacent liver tissues from CDAHFD (disease) and SD (control) mice, stained with H&E, Sirius Red, or Prussian Blue. (*E*) Liver collagen concentration assessed by hydroxyproline content (Hyp, μg/g tissue) ($n = 6$ for each group). (*F*) Collagen proportional area (CPA) measured from Sirius Red-stained tissue ($n = 6$ for each group). (*G*) Quantitative analyses of fat content in H&E-stained livers of CDAHFD and control mice ($n = 6$ for each group). All data shown as mean ± SD, $^{**}P < 0.01$, $^{***}P < 0.001$, unpaired *t* test, two-tailed.

collagen network as revealed by Sirius Red staining. The liver hydroxyproline level was higher in CDAHFD mice than in SC mice (630 ± 200 μg/g tissue vs. 110 ± 24 μg/g tissue) (Fig. 4*E*), in agreement with increased collagen deposition in CDAHFD mice, as assessed by CPA from Sirius Red staining (7.9 ± 3.0% in CDAHFD vs. 0.1 ± 0.1% in control mice) (Fig. 4*F*), confirming the presence of fibrosis in CDAHFD mice. Morphometric quantification of steatosis also showed a significantly higher fat percentage in the CDAHFD group (28.5 ± 4.4% vs. 1.5 ± 0.4% in SC mice from H&E-stained slices, Fig. 4*G*).

Discussion

We opted for an SNIO/CBP ratio close to 1/1 for the design of the conjugated nanoparticles. Increasing the ratio of CBP to iron increases the particle hydrodynamic diameter, which could result in extended blood half-life, lower clearance by the kidneys, and potentially a larger degree of tissue retention and nonspecific signal enhancement in the liver. Hydrophobicity of the peptide also had a negative effect on the solubility of the nanoparticles in water. Based on these considerations, a formulation with an SNIO/CBP ratio of 1/1.1 was used in this study to ensure that SNIO nanoparticles smaller than the mean size were also functionalized.

Notably, after modification with CBP, SNIO–CBP showed higher longitudinal relaxivity than unmodified SNIO, and it is six times higher than CM-101 under the same peptide concentration at 4.7 T. The dissociation constant for binding to human type I collagen was 18.4 μM for SNIO–CBP, which was 5.1 times higher than that for CM-101 (3.6 μM). The lower affinity of SNIO–CBP is likely due to steric hindrance caused by the iron oxide nanoparticles. Despite the lower collagen affinity for SNIO–CBP, its 6.7-fold higher relaxivity than CM-101 enabled SNIO–CBP to detect liver fibrosis with comparable sensitivity to CM-101 at a 2.5-fold lower dose as confirmed by the animal studies. The blood half-life of SNIO–CBP in normal mice (5.7 ± 1.9 min) was similar to gadolinium-based small molecules and much shorter than reported SPIONs of larger sizes, consistent with efficient renal filtration.

In vivo results demonstrated that SNIO–CBP detected liver fibrosis using T_1-weighted MRI in both toxin-induced and diet-induced mouse models of liver fibrosis. The liver contrast enhancement was read out within 15 min after injection; a time that is significantly shorter than the readout with most nanoparticle agents. Moreover, the liver background signal was much lower than that of other nanoparticles thanks to the extremely small particle size of SNIO–CBP. Prussian Blue staining together with Sirius Red staining showed a strong correlation between SNIO–CBP and collagen deposition in fibrotic liver tissues. The correlation confirmed the binding specificity of SNIO–CBP to collagen. The observation of iron accumulation in the liver suggested that nanoparticle clearance within our total imaging timeframe of less than 40 min was incomplete, which may be due to the slower washout rate upon binding.

This study demonstrates several conceptual advances for molecular MR imaging. It has long been recognized that signal generation is a limitation of molecular targeting with MR. While nanotechnology approaches can provide very high payloads of imaging reporters (7), they are typically limited by unfavorable pharmacokinetics: long blood circulation times, retention in liver, and slow extravasation out of the vascular compartment into the interstitium (15). As a result, hours to days are required to accumulate enough probe at the site of interest. These long times have limited the clinical translation of such molecular probes (38). On the other hand, the synthesis of discrete probes with multiple gadolinium chelates conjugated to a targeting vector has proven useful in some instances (39, 40), but this approach suffers from synthetic complexity resulting in a high cost of manufacturing (41). In this work, we show that the SNIO platform offers a synthetically straightforward approach to delivering a large payload of ferric ions with high relaxivity by readily functionalizing the SNIO with a peptide or small molecule to provide molecular targeting. We have demonstrated that SNIO–CBP-enhanced MRI can detect liver fibrosis within minutes of administration; a time frame that is compatible with clinical imaging protocols. This SNIO framework is readily adapted to other targeting vectors that have been utilized in other molecular MR applications (2, 5, 41).

In summary, collagen-binding SNIO nanoparticles, SNIO–CBP, with near 1/1 SNIO/CBP stoichiometry, were successfully formulated. The SNIOs act as both reporters for MRI contrast and carriers for delivering the CBP vector for collagen targeting. We confirmed the ability of SNIO–CBP to act as a T_1-weighted MRI contrast agent through longitudinal relaxivity measurements, demonstrated the binding affinity of SNIO–CBP toward human type I collagen in vitro, and obtained its pharmacokinetic profile using T_1-weighted MRI in mice. As a gadolinium-free platform with high renal clearance and low nonspecific liver uptake, we further demonstrated the ability of SNIO–CBP enhanced MRI to detect liver fibrosis in two mouse models. Drawing a parallel between the newly formulated SNIO–CBP and the molecular collagen-targeting CM-101, we observed similar results for the two contrast agents when the dosage of SNIO–CBP was 2.5 times lower per peptide. With the methodology established in this report, we provide an approach to functionalize SNIO nanoparticles, which have endogenous atomic elements, superior magnetic properties, and small molecule-like pharmacokinetics, for broader application. Our study thus brings us one step closer toward gadolinium-free targeted MRI in the clinical setting.

Materials and Methods

Unless specified, all chemicals were purchased from MilliporeSigma.

SNIO Nanoparticles with Oleic Acid Surface Ligands (SNIO–OA). SNIO–OA was synthesized according to previous report, except that the final product was dispersed in toluene instead of hexanes (20).

Propargyl Dihydrocaffeic Acid (PDA). PDA was synthesized according to a modified procedure (42). In a 250-mL round-bottom flask, to the solution of dihydrocaffeic acid (1.82 g, 10 mmol) in tetrahydrofuran (100 mL) were added *N*,*N*′-dicyclohexylcarbodiimide (2.27 g, 11 mmol) and *N*-hydroxysuccinimide (1.27 g, 11 mmol). The mixture was stirred at room temperature under nitrogen for 2 h and was filtered. To the filtrate solution under nitrogen were added propargylamine (0.55 g, 10 mmol) and triethylamine (1.01 g, 10 mmol), and the solution was stirred at room temperature for 24 h. The mixture was filtered again, concentrated in vacuo, loaded on a silica column, and then washed with 15% methanol in dichloromethane to give a yellow viscous oil (reaction yield 90%). The product was stored at room temperature and under nitrogen.

Alkyne Functionalization of SNIO Nanoparticles (SNIO–Alkyne). The following method describes the preparation of SNIO–alkyne at a scale suitable for imaging 10 to 12 mice at a dosage described in this report. In a 7-mL scintillation vial, SNIO–OA in toluene (1 mL), 2-(2-methoxyethoxy)acetic acid (1 mL, TCI America), and toluene (2 mL) were added. The vial was capped, and the solution was stirred at 70 °C for 15 min. After cooling to room temperature, the resulting solution was transferred into a centrifuge tube, and hexanes (20 mL) were added, resulting in a two-phase system. Acetone was then added in small amounts until a highly concentrated bottom phase was obtained. Centrifugation can be used to help phase separation. Meanwhile, in a 50-mL round-bottom flask, 50 mg PDA and 750 mg ZDS were dispersed in a mixture of 10 mL DMF and 5 mL water. The product was carefully pipetted and added to the solution mixture. The reaction mixture was stirred at 70 °C for 6 h under nitrogen. After cooling down to room temperature, the SNIO–alkyne mixture was precipitated with 30 mL acetone. After centrifugation, the supernatant was discarded, and the remaining pellet was dispersed in sodium phosphate buffer (10 mL, 10 mM phosphates, pH 7.4, without saline), concentrated to 1 mL through centrifugal filtration (MWCO 3000 Da, Amicon) five to seven times until the filtrate became lightly purple, filtered through Nylon syringe filter (0.22 μm, Millipore Millex) and stored at 4 °C. The iron content was analyzed through ^{56}Fe ICP-MS with ^{45}Sc as an internal standard on an Agilent 7900 inductively coupled plasma mass spectrometry ICP-MS. This method has been scaled up to as much as 4 mL of SNIO–OA as the starting material or down to 25 μL of SNIO–OA.

[(Benzimidazol-2-yl)methyl]bis[(2-pyridylmethyl)]amine (BPBA). BPBA (also known as BimPy2) was prepared according to literature methods (30). The reaction yield was 42%. Off-white crystals were stored at room temperature under nitrogen.

Azide-Functionalized CBP–Azide. CBP–azide was obtained through azide functionalization of the N-terminus of the unfunctionalized CBP (AmbioPharm). N_3-PEG_6-COOH (200.0 mg, 0.53 mmol, BroadPharm) (PEG: polyethylene glycol), pentafluorophenol (PFP, 155.3 mg, 0.84 mmol), and PS-carbodiimide resin (503 mg, 0.84 mmol) were taken together in a reaction vessel with a magnetic stirring bar. Dichloromethane (5 mL) was added, and the reaction mixture was allowed to stir at room temperature for 3 h. The reaction progress was monitored by high-performance liquid chromatography–mass spectrometry (HPLC–MS). Upon completion of the reaction, the mixture was filtered off to remove the PS-carbodiimide resin and the resulting solution was evaporated under reduced pressure to remove dichloromethane. The activated ester N_3-PEG_6-COOPFP was isolated as a pale yellow solid and was used as is for the next step. To the solution of CBP (50 mg, 0.02 mmol) in DMF was added N_3-PEG_6-COOPFP (12 mg, 0.02 mmol). The pH was maintained at 9 by the addition of *N*,*N*-diisopropylethylamine and the reaction was allowed to stir at room temperature. Upon completion of the reaction as observed by liquid chromatography–mass spectrometry (LC–MS), the reaction mixture was poured into a falcon tube containing cold diethyl ether to precipitate the coupled product. The solution was centrifuged, and the residue was isolated as the crude peptide-PEG linker conjugate. The crude compound was isolated by preparatory HPLC to obtain the off-white solid, CBP-azide. CBP-azide was characterized by LC–MS (Agilent 1260 system coupled to an Agilent Technologies 6130 Quadrupole MS system; 5 to 95%, 0.1% Formic acid ACN/0.1% Formic acid water; Phenomenex LUNA, C18(2), 5 μm, 100 × 2 mm, flow rate: 0.7 mL/min): t_R = 4.92 min; purity > 95%; *m*/*z*, [*M*+2]/2 = 1280.3, [*M*+3]/3 = 254.3.

SNIO Nanoparticles Conjugated with CBP (SNIO–CBP). In a 5-mL round-bottom flask, CBP–azide (10 mg) was dissolved in dimethylsulfoxide (DMSO, 3.2 mL). Separately, SNIO–alkyne (65 μmol Fe per ICP-MS) was concentrated through centrifugal filtration (Molecular weight cut-off (MWCO) 3000 Da) to 500 μL and added into the solution above. Water (60 μL) was added to help transfer SNIO–alkyne solution. The flask was placed under a vacuum, then filled with nitrogen, three times on Schlenk line. Meanwhile, in a microcentrifuge tube, copper sulfate in water (30 μL, 20 mM), BPBA in DMSO (30 μL, 40 mM), and sodium ascorbate in water (300 μL, 100 mM) were combined. Then, 240 μL of the mixture was injected into the reaction mixture through a syringe. The flask was placed under a vacuum and filled with nitrogen three times. The reaction mixture was stirred at 25 °C for 2 h, precipitated with 30 mL acetone, and redispersed in sodium phosphate buffer (10 mL, 10 mM phosphates, pH 7.4, without saline). The product was concentrated to 1 mL through centrifugal filtration (MWCO 3000 Da) three times, filtered through a Nylon syringe filter (0.22 μm) and stored at 4 °C. The iron content was analyzed through ^{56}Fe ICP-MS with ^{45}Sc as an internal standard; the peptide concentration was analyzed through *L*-amino acid analysis as described below.

X-ray Scattering Analysis. X-ray scattering data were collected with momentum transfer q 0.40~10 nm^{-1} on an absolute scale in transmission mode with Cu K-alpha emission at 1.5418 Å (Rigaku 002 Microfocus X-ray source, Rigaku) and Dectris PILATUS3 R 300K detector (Dectris USA) on a SAXSLAB system (Skovlunde), integrated over 300 s. An SNIO–CBP sample in 10 mM pH 7.4 sodium phosphate buffer was loaded in a 1.5-mm quartz capillary (Hampton Research) and sealed with sealing wax (Hamilton Research). Background signal of the solvent was also collected under the same conditions and subtracted from the data for SNIO–CBP for processing. Data processing was performed on SasView5 software using a spherical particle model with a log-normal distribution.

Gel Filtration Chromatography (GFC). GFC on Superose 12 10/300 GL high-performance size exclusion column (General Electric) was performed on the ÄKTAprime Plus FPLC system used in accordance with protocols in our previous report (20). A reconstituted gel filtration standard (Bio-rad, #1511901) was used to calibrate the column for hydrodynamic diameter correlation. A hydrodynamic diameter (d_{HD}, nm)–elution time (t, min) relationship was fit into a quadratic equation $d_{HD} = 0.0264t^2 - 2.213t + 47.96$ ($R^2 = 0.9917$). The elution time of SNIO–CBP was 31.1 min, giving a hydrodynamic diameter of 4.6 nm.

***L*-amino Acid Analysis.** An SNIO–CBP stock solution (36 mM Fe, 50 μL) was added to a 5-mL round-bottom flask and was digested with 1 mL of 6 M HCl for 24 h under nitrogen protection. After cooling to room temperature, the solution was evaporated in vacuo, leaving a black residue. Then, 1 × pH 7.4 phosphate-buffered saline (PBS) (200 μL) was added, and the mixture was transferred into a microcentrifuge tube and centrifugated at 10k rpm for 5 min. Following that, 100 μL of the supernatant was collected and was diluted with 100 μL Tris-acetate-EDTA buffer. This final solution approximately contained 1 mM total *L*-amino acids. Enzymatic fluorometric quantification (excitation wavelength $\lambda_{ex} = 535$ nm, emission wavelength $\lambda_{em} = 587$ nm) was performed with an *L*-amino Acid Quantification Kit (Sigma-Aldrich, MAK002). CBP concentration is 1/14 of total *L*-amino acid concentration (glycine and tryptophan are not detected by this method).

Nonspecific Binding with Plasma. An aliquot of SNIO–CBP stock solution was taken and diluted with 1 × pH 7.4 PBS, and FBS was added. The final solution was 200 μL in volume, contained 6 mM SNIO–CBP on a per-Fe basis and 10% FBS. The mixture was incubated at 37 °C for 5 min and a size exclusion chromatogram was taken. Chromatograms of SNIO–CBP with 20% FBS and 20% FBS without SNIO–CBP were taken successively after the same amount of incubation time. The iron concentration and the incubation period were designed in accordance with the concentration and half-life of SNIO–CBP in mouse blood pool.

Type I Collagen Binding Affinity. The collagen binding procedure was performed in vitro similar to our previous report (26). Aliquots of Human type I collagen solution were placed into half of the wells of a 96-well plate, gelled, and dried, forming thin films on the plate bottom. The final content of gelled collagen in each well was 150 μg. A series of SNIO–CBP dilutions in 1 × pH 7.4 PBS ranging from 0.1 to 35 mM on a per-CBP basis were made from stock solution. Each dilution was added into one well containing collagen and one well without collagen; the volume of each addition was 90 μL. The 96-well plate was gently shaken at room temperature for 2 h without disturbing the collagen films on the bottom, 45 μL supernatants were collected, and the content of contrast agents in the supernatants were measured with ^{56}Fe ICP-MS. For each dilution, the difference in CBP concentration between the well containing collagen and the well without collagen indicated the portion of SNIO–CBP bound to collagen.

For each dilution, CBP concentration in the well without collagen was noted as $[CBP]_0$, and the concentration in the well with collagen film was noted as [CBP]. CBP bound with collagen [CBP–collagen] = $[CBP]_0 - [CBP]$. For the binding reaction CBP + collagen ⇌ CBP–collagen, the dissociation constant K_d was extracted through fitting the experiment data with the Langmuir isotherm model

$$[\text{CBP} - \text{collagen}] = \frac{[\text{collagen}]_0[\text{CBP}]}{K_d + [\text{CBP}]}. \quad [\mathbf{1}]$$

Data fitting gave $K_d = 18.4$ μM ($R^2 = 0.9982$). Numeric data are provided in *SI Appendix*.

Longitudinal Relaxivities. CM-101 and SNIO–CBP at a range of concentrations (0.01 to 0.2 mM) were prepared in 1 × pH 7.4 PBS. For relaxivity at 1.41 T, longitudinal (T_1) relaxation times were measured via an inversion recovery experiment using 10 inversions of duration ranging between 0.05 T_1 and 10 T_1 on a Bruker mq60 Minispec at 1.41 T and 37 °C. Relaxivities at 4.7 T were measured on a 4.7 Tesla MRI scanner (Bruker) using a custom-built volume coil with T_1 mapping FARE sequence. Then, the concentration of the corresponding metal ions was determined on an Agilent 7900 ICP-MS. The relaxivity r_1 was then determined from the slope of a plot of 1/ T_1 vs. metal concentration for five concentrations.

Animal Studies. All animal experiments were performed in accordance with the NIH Guide for the Care and Use of Laboratory Animals and in compliance with the ARRIVE guidelines and approved by the MGH Institutional Animal Care and Use Committee. A total of 35 mice were studied. No animals were excluded from the study.

CCl_4 Liver Fibrosis Mouse Model. Male C57BL/6 mice (6-wk-old, Charles River Laboratories) were treated with an oral gavage of carbon tetrachloride for 12 wk (two to three times per week, 0.1 mL of 20% CCl_4 in olive oil the first week, 30% the second week, and 40% from weeks 3 through 12). Control mice were treated with vehicle (olive oil) only.

Group 1, CCl_4 for 12 wk ($n = 6$) and imaged with SNIO–CBP (2 nmol/g CBP).

Group 2, CCl_4 for 12 wk ($n = 6$) and imaged with CM-101 (5 nmol/g CBP).

Group 3, vehicle-treated control ($n = 4$) and imaged with SNIO–CBP (2 nmol/g CBP).

Group 4, vehicle-treated control ($n = 4$) and imaged with CM-101 (5 nmol/g CBP).

CDAHFD Mouse Model. A total of 20 C57BL/6 mice were used in this study and randomized to each study group. To induce NASH, 6-wk-old, male C57BL/6 mice (Charles River Labs) were fed CDAHFD ($n = 6$) consisting of 60 kcal% fat and 0.1% methionine by weight (A06071302; Research Diets) for 14 wk. Another group of gender and age-matched mice were fed SC for 14 wk.

MR Imaging. Animals were anesthetized with isoflurane (1 to 2%) and placed in a specially designed cradle with body temperature maintained at 37 °C. Inhaled isoflurane level was adjusted to maintain a respiration rate of 60 ± 5 breaths per minute. The tail vein was cannulated for intravenous delivery of the corresponding probe while the animal was positioned in the scanner. Imaging was performed at 4.7 T using a small bore animal scanner with a custom-built volume coil. A series of baseline images [3D T_1-weighted fast low angle shot MRI (FLASH)] were first acquired (repetition time/echo time = 15/2 ms; flip angle, 30°; field of view, 48 × 30 mm^2; matrix size, 136 × 136; slice thickness, 0.25 mm; acquisition time, 3 min 20 s), then a bolus of molecular probe was administered intravenously and imaging was performed for a period of 35 min postinjection by repeating 3D T_1 -weighted FLASH sequences. Following the imaging session, animals were killed (40 min postinjection) and liver tissues were subjected to histopathologic analysis.

MRI Data Analysis. A region of interest (ROI) was manually traced encompassing the liver parenchyma while avoiding major blood vessels. A second ROI was placed on the dorsal muscle visible in the same image slice to quantify the signal intensity in the muscle for comparison. Seven ROIs were placed in the field of view without any tissue (air) to measure the variation in background signal. The same analysis was performed on the preinjection and 35 min postinjection images acquired with the FLASH sequence. Image visualization and quantification were performed in Horos software. Contrast-to-noise ratio (CNR) was calculated by subtracting the signal intensity (SI) in the muscle from that in the liver and normalizing to the SD of the signal in the air outside the animal, Eq. **2**. Changes in contrast-to-noise ratio CNR were calculated by subtracting the CNR_{pre} from CNR_{post}, Eq. **3**.

$$\text{CNR} = \left(\text{SI}_{\text{liver}} - \text{SI}_{\text{muscle}}\right) / \text{SD}_{\text{air}}, \quad [\mathbf{2}]$$

$$\Delta\text{CNR} = \text{CNR}_{\text{post}} - \text{CNR}_{\text{pre}}. \quad [\mathbf{3}]$$

Histopathology Procedures. After imaging, the mice were killed under anesthesia, and the liver tissues were collected. A piece of the left lobe of the liver was immediately fixed in 4% buffered paraformaldehyde, dehydrated, embedded in paraffin, and then sectioned into 5-μm-thick slices for staining with Sirius red, hematoxylin and eosin (H&E), and Prussian Blue (Abcam, ab150674). Another piece of left lobe was quickly frozen in liquid nitrogen for hydroxyproline analysis, which was quantified by a reported HPLC analysis method (43). The hydroxyproline in liver was then expressed as amounts per wet weight of tissue. The collagen proportional area (CPA), defined as the percentage of the area stained positive by Sirius red, was measured with ImageJ (Fiji, version 1.0) as previously described (28). For NASH study, H&E sections were evaluated and morphometric quantitation of hepatic steatosis, expressed as percentage of lipid vacuolization, was performed using ImageJ (Fiji, version 1.0).

Data, Materials, and Software Availability. All study data are included in the article and/or *SI Appendix*.

ACKNOWLEDGMENTS. J.Z. acknowledges support from Laser Biomedical Resource Center, NIH (2-P41-EB015871-31). V.H. received funding from National Institute for Biomedical Imaging and Bioengineering (R43EB030959). P.C. received funding from National Institute of Diabetes and Digestive and Kidney Diseases (DK121789) and NIH Office of the Director (OD025234, OD010650, and OD032138). H.Z. acknowledges support from the NSF (CHE-2108357) for his contribution in the synthesis and physical characterizations. This work also benefited from the use of the SasView application, originally developed under NSF award DMR-0520547. SasView contains code developed with funding from the European Union's Horizon 2020 research and innovation programme under the SINE2020 project, grant agreement No 654000.

Author affiliations: [a]Department of Chemistry, Massachusetts Institute of Technology, Cambridge, MA 02139; [b]Athinoula A. Martinos Center for Biomedical Imaging, Institute for Innovation in Imaging, Department of Radiology, Massachusetts General Hospital, Harvard Medical School, Boston, MA 02129; [c]Department of Biological Engineering, Massachusetts Institute of Technology, Cambridge, MA 02139; [d]Collagen Medical, Boston, MA 02478; and [e]Division of Gastrointestinal and Oncological Surgery, Massachusetts General Hospital, Harvard Medical School, Boston, MA 02114

Author contributions: J.Z., Y.N., P.C., and M.G.B. designed research; J.Z., Y.N., H.Z., H.W., H.D., E.C.H., I.Y.Z., S.C.B., M.S., K.K.T., and V.H. performed or assisted in research; J.Z., Y.N., N.J.R., H.W., H.D., V.H., A.J., P.C., and M.G.B. contributed new reagents/analytic tools; J.Z., Y.N., H.Z., N.J.R., H.W., H.D., I.Y.Z., S.C.B., M.S., K.K.T., P.C., and M.G.B. analyzed data or assisted in data analysis; and J.Z., Y.N., P.C., and M.G.B. wrote the paper.

Reviewers: S.S., Brown University; and M.F.T., The Ohio State University.

Competing interest statement: P.C. is a consultant to Collagen Medical LLC. H.D. and V.H. are employees of Collagen Medical LLC. P.C. has equity in Collagen Medical LLC and Reveal Pharmaceuticals Inc. A patent application related to this work is being filed. In addition, the authors hold the patent of US Patent and Trademark Office Application 16/184,379 (Tiny nanoparticles for magnetic resonance imaging applications). P.C. has research support from Pliant Therapeutics, Takeda, and Janssen. Reviewer M.F.T. sits on the scientific advisory board of Reveal Pharmaceuticals with one of the authors (P.C.) and owns stock.

1. A. S. Merbach, L. Helm, E. Toth, *The Chemistry of Contrast Agents in Medical Magnetic Resonance Imaging* (John Wiley & Sons, 2013).
2. J. Wahsner, E. M. Gale, A. Rodriguez-Rodriguez, P. Caravan, Chemistry of MRI contrast agents: Current challenges and new frontiers. *Chem. Rev.* **119**, 957–1057 (2019).
3. E. Kanal, Gadolinium based contrast agents (GBCA): Safety overview after 3 decades of clinical experience. *Magn. Reson. Imaging* **34**, 1341–1345 (2016).
4. R. J. McDonald *et al.*, Gadolinium retention: A research roadmap from the 2018 NIH/ACR/RSNA workshop on Gadolinium Chelates. *Radiology* **289**, 517–534 (2018).
5. H. Li, T. J. Meade, Molecular magnetic resonance imaging with Gd(III)-based contrast agents: Challenges and key advances. *J. Am. Chem. Soc.* **141**, 17025–17041 (2019).
6. J. Lux, A. D. Sherry, Advances in gadolinium-based MRI contrast agent designs for monitoring biological processes in vivo. *Curr. Opin. Chem. Biol.* **45**, 121–130 (2018).
7. H. B. Na, I. C. Song, T. Hyeon, Inorganic nanoparticles for MRI contrast agents. *Adv. Mater.* **21**, 2133–2148 (2009).
8. Z. Shen, A. Wu, X. Chen, Iron oxide nanoparticle based contrast agents for magnetic resonance imaging. *Mol. Pharm.* **14**, 1352–1364 (2017).
9. N. Lee, T. Hyeon, Designed synthesis of uniformly sized iron oxide nanoparticles for efficient magnetic resonance imaging contrast agents. *Chem. Soc. Rev.* **41**, 2575–2589 (2012).
10. R. Qiao, C. Yang, M. Gao, Superparamagnetic iron oxide nanoparticles: From preparations to in vivo MRI applications. *J. Mater. Chem.* **19**, 6274–6293 (2009).
11. R. Jin, B. Lin, D. Li, H. Ai, Superparamagnetic iron oxide nanoparticles for MR imaging and therapy: Design considerations and clinical applications. *Curr. Opin. Pharmacol.* **18**, 18–27 (2014).
12. M. Jeon, M. V. Halbert, Z. R. Stephen, M. Zhang, Iron oxide nanoparticles as T_1 contrast agents for magnetic resonance imaging: Fundamentals, challenges, applications, and prospectives. *Adv. Mater.* **33**, e1906539 (2021).
13. Z. Zhou, L. Yang, J. Gao, X. Chen, Structure-relaxivity relationships of magnetic nanoparticles for magnetic resonance imaging. *Adv. Mater.* **31**, e1804567 (2019).
14. Y. N. Zhang, W. Poon, A. J. Tavares, I. D. McGilvray, W. C. W. Chan, Nanoparticle-liver interactions: Cellular uptake and hepatobiliary elimination. *J. Control. Release* **240**, 332–348 (2016).
15. F. M. Kievit, M. Zhang, Surface engineering of iron oxide nanoparticles for targeted cancer therapy. *Acc. Chem. Res.* **44**, 853–862 (2011).
16. J. Li, C. Chen, T. Xia, Understanding nanomaterial-liver interactions to facilitate the development of safer nanoapplications. *Adv. Mater.* **34**, e2106456 (2022).
17. H. Wei *et al.*, Compact zwitterion-coated iron oxide nanoparticles for biological applications. *Nano Lett.* **12**, 22–25 (2012).
18. H. Wei, O. T. Bruns, O. Chen, M. G. Bawendi, Compact zwitterion-coated iron oxide nanoparticles for in vitro and in vivo imaging. *Integr. Biol.* **5**, 108–114 (2013).
19. H. Wei *et al.*, Exceedingly small iron oxide nanoparticles as positive MRI contrast agents. *Proc. Natl. Acad. Sci. U.S.A.* **114**, 2325–2330 (2017).
20. H. Wei *et al.*, Single-nanometer iron oxide nanoparticles as tissue-permeable MRI contrast agents. *Proc. Natl. Acad. Sci. U.S.A.* **118**, e2102340118 (2021).
21. N. Roehlen, E. Crouchet, T. F. Baumert, Liver fibrosis: Mechanistic concepts and therapeutic perspectives. *Cells* **9**, 875 (2020).
22. T. Kisseleva, D. Brenner, Molecular and cellular mechanisms of liver fibrosis and its regression. *Nat. Rev. Gastroenterol. Hepatol.* **18**, 151–166 (2021).
23. K. Patel, G. Sebastiani, Limitations of non-invasive tests for assessment of liver fibrosis. *JHEP Rep.* **2**, 100067 (2020).
24. I. Y. Zhou, O. A. Catalano, P. Caravan, Advances in functional and molecular MRI technologies in chronic liver diseases. *J. Hepatol.* **73**, 1241–1254 (2020).
25. E. B. Tapper, A. S. Lok, Use of liver imaging and biopsy in clinical practice. *N. Engl. J. Med.* **377**, 756–768 (2017).
26. P. Caravan *et al.*, Collagen-targeted MRI contrast agent for molecular imaging of fibrosis. *Angew. Chem. Int. Ed.* **46**, 8171–8173 (2007).
27. B. C. Fuchs *et al.*, Molecular MRI of collagen to diagnose and stage liver fibrosis. *J. Hepatol.* **59**, 992–998 (2013).
28. C. T. Farrar *et al.*, CM-101: Type I collagen-targeted MR imaging probe for detection of liver fibrosis. *Radiology* **287**, 581–589 (2018).
29. M. Salarian *et al.*, Early detection and staging of chronic liver diseases with a protein MRI contrast agent. *Nat. Commun.* **10**, 4777 (2019).
30. M. Pascaly *et al.*, The systematic influence of tripodal ligands on the catechol cleaving activity of iron(III) containing model compounds for catechol 1,2-dioxygenases. *J. Chem. Soc. Dalton Trans.* **6**, 828–837 (2001).
31. S. I. Presolski, V. Hong, S. H. Cho, M. G. Finn, Tailored ligand acceleration of the Cu-catalyzed azide-alkyne cycloaddition reaction: Practical and mechanistic implications. *J. Am. Chem. Soc.* **132**, 14570–14576 (2010).
32. J. Baumgartner *et al.*, Self-confined nucleation of iron oxide nanoparticles in a nanostructured amorphous precursor. *Nano Lett.* **20**, 5001–5007 (2020).
33. H. S. Choi *et al.*, Renal clearance of quantum dots. *Nat. Biotechnol.* **25**, 1165–1170 (2007).
34. E. C. Hulme, M. A. Trevethick, Ligand binding assays at equilibrium: Validation and interpretation. *Br. J. Pharmacol.* **161**, 1219–1237 (2010).
35. D. J. Erstad *et al.*, Fibrotic response to neoadjuvant therapy predicts survival in pancreatic cancer and is measurable with collagen-targeted molecular MRI. *Clin. Cancer Res.* **26**, 5007–5018 (2020).
36. D. Scholten, J. Trebicka, C. Liedtke, R. Weiskirchen, The carbon tetrachloride model in mice. *Lab. Anim.* **49**, 4–11 (2015).
37. M. Matsumoto *et al.*, An improved mouse model that rapidly develops fibrosis in non-alcoholic steatohepatitis. *Int. J. Exp. Pathol.* **94**, 93–103 (2013).
38. T. Skotland, T. G. Iversen, K. Sandvig, New metal-based nanoparticles for intravenous use: Requirements for clinical success with focus on medical imaging. *Nanomedicine* **6**, 730–737 (2010).
39. K. Overoye-Chan *et al.*, EP-2104R: A fibrin-specific gadolinium-based MRI contrast agent for detection of thrombus. *J. Am. Chem. Soc.* **130**, 6025–6039 (2008).
40. Z. Zhou *et al.*, MRI detection of breast cancer micrometastases with a fibronectin-targeting contrast agent. *Nat. Commun.* **6**, 7984 (2015).
41. S. Shuvaev, E. Akam, P. Caravan, Molecular MR contrast agents. *Invest. Radiol.* **56**, 20–34 (2021).
42. L. Li, Y. Li, X. Luo, J. Deng, W. Yang, Helical poly (N-propargylamide) s with functional catechol groups: Synthesis and adsorption of metal ions in aqueous solution. *React. Funct. Polym.* **70**, 938–943 (2010).
43. P. R. Hutson, M. E. Crawford, R. L. Sorkness, Liquid chromatographic determination of hydroxyproline in tissue samples. *J. Chromatogr. B* **791**, 427–430 (2003).